Secondary-electron yields and their dependence on the angle of incidence on stainless-steel surfaces for three energetic ion beams

P. Thieberger,* A. L. Hanson, D. B. Steski, V. Zajic, S. Y. Zhang, and H. Ludewig
Brookhaven National Laboratory, Upton, New York 11973
(Received 24 August 1999; published 15 March 2000)

Secondary-electron yields were investigated for 28-MeV protons, 126-MeV oxygen-ions, and 182-MeV gold ions incident on 304 stainless-steel surfaces. The dependence on the incidence angle was studied in detail, and a system was developed which allows accurate measurements to be performed over a wide angular range extending to nearly grazing collisions. Electron yield estimates of interest for future accelerator applications are developed for 1-GeV protons, and the possible mitigation of deleterious effects by using serrated rather than flat surfaces is analyzed.

PACS number(s): 79.20.Rf, 34.90.+q.

I. INTRODUCTION

There is considerable experimental information available for the yield of secondary electrons ejected following the impact of a variety of ions on different solid surfaces and also at the exit surfaces for ions penetrating thin targets. The field has been recently reviewed by several authors [1–4]. There are relatively few measurements for energies larger than 1 MeV/amu and of these, most are performed at normal incidence. Near grazing collisions are of particular importance for the practical applications described below. They are also of interest for the understanding of the underlying phenomena, since the yields (which become very large) are known, at lower energies, to deviate markedly from predictions based on semiempirical theories.

The present experiments were motivated by the need to evaluate (and eventually avoid or mitigate) deleterious effects of secondary electrons on ion accelerator performance. In particular, e-p instabilities could occur in the Spallation Neutron Source (SNS) now in the design stage, if large numbers of electrons are generated through grazing collisions of halo protons with the surfaces of the collimators, which are an essential part of the SNS ring design [5]. Also, loading effects noticed at the Alternating Gradient Synchrotron (AGS) Booster inflector when 1-MeV/amu gold beams are injected are clearly due to secondary electrons. In fact, one of us (S. Y. Zhang) recently performed measurements of this effect [6] and arrived at preliminary yield estimates for grazing collisions of 1-MeV/amu gold ions with a stainless-steel surface. There are very few other measurements of electron yields for stainless steel (SS) in the literature, and only at much lower energies (see, e.g., Ref. [7]). This material was chosen for the present work because of its importance for the accelerator applications and also because it allows one to largely avoid the issue of surface oxide layers drastically influencing the results under realistic vacuum conditions.

For ion energies of interest here (>100 KeV/amu) almost all of the electrons emitted into the vacuum following the ion entrance into (or the exit from) a solid surface come from within the solid. The production of these electrons can be described as a three-step process [2]. First the incoming ion transfers energy to electrons in the solid at a rate given by $(dE/dx)_e$ the electronic stopping power, which for the ions of interest here is by far the largest part of the total stopping power (see Table III below). Second, the electrons scatter and cascade, multiplying and diffusing through the solid. The electrons emitted from the ion entrance surface are thought to be mainly due to soft collisions leading to low-energy electrons [8]. Finally, a small fraction of these low-energy electrons, mostly originating from an escape zone or surface layer, which, e.g., for carbon is typically ~30 Å thick [8], manage to penetrate the surface potential barrier escaping into the vacuum. According to Ref. [8], the diffusion length of these low-energy electrons should mainly depend on the target material and not so much on the projectile atomic number or velocity. Since the escape zone is so thin, the electronic stopping power relevant for the escaping electrons can be evaluated at the incident ion energy.

To the extent that the above picture is valid, one can expect [9,10] the thick target backward yield γ_B (i.e., mean number of electrons emitted backwards per incident ion) to be

$$\gamma_B = \Lambda_M \beta_S \left(\frac{dE}{dx}\right)_e \cos^{-1}(\theta), \tag{1}$$

where Λ_M is a constant for a given material, and θ is the angle of incidence with respect to a line perpendicular to the surface. $\beta_S = 1 - \beta_\delta$ is the partition factor for ''soft'' collisions which describes the fraction of the projectile energy lost directly to low-energy electrons, and β_δ is the fraction lost in close collisions leading to the more energetic δ electrons. These δ electrons are mostly forward directed and are therefore thought to make a negligible contribution to the backward yield γ_B. Sternglass [11] had assumed an equipartition between both types of collisions for fast projectiles, i.e., $\beta_S = \beta_\delta = 0.5$ which would lead to a Meckbach factor [12] $\gamma_F/\gamma_B = 2$, where γ_F is the forward yield. Experimental values of this ratio are usually smaller, e.g., ~1.2 for protons of 0.02–9.5 MeV on carbon targets [10].

*Author to whom correspondence should be addressed. Electronic address: pt@bnl.gov

Equation (1), especially for $\theta=0°$, holds fairly well for protons over a wide energy range extending, e.g., from 0.02 to 7.5 MeV for carbon targets [13] and from 15 to 68 MeV for an Al_2O_3 target [14]. Deviations which are encountered for heavier ions both in yield at normal incidence and in angular dependence can be parametrized as follows [15,2]:

$$\gamma_B(\theta)=\gamma_B(0°)\cos^{-f}(\theta)=C_B\Lambda_B^{Z=1}\left(\frac{dE}{dx}\right)_e\cos^{-f}(\theta), \tag{2}$$

where, by definition, $C_B=1$ for protons, and $\Lambda_B^{Z=1}$ is the ratio $\gamma_B^{Z=1}(0°)/(dE/dx)_e$ for protons at normal incidence. As mentioned above, for a given target material, this ratio has been found to be fairly constant over several orders of magnitude in energy. $\Lambda_B^{Z=1}$ is therefore a parameter characteristic of each material. The ratio $\gamma_B(0°)/(dE/dx)_e$ for other ions is usually smaller than for protons and such ''deficits'' are reflected in values of $C_B<1$. Deviations from the simple description summarized in Eq. (1) will thus be quantified as values of the parameters $C_B\neq 1$ and $f\neq 1$.

Several possible causes have been mentioned in the literature for values of $C_B<1$, i.e., for less efficient energy conversion into backscattered electrons for heavy ions as compared to protons [2,10]. One explanation is based on the fact that, while traversing the thin escape zone, the ion usually is far from the equilibrium charge state, and therefore the effective value of $(dE/dx)_e$ will in general be different (usually smaller) than the bulk value. Such near-surface nonequilibrium stopping-power effects have in fact been observed with ions of equal velocities and different charge states [9].

Describing the deviation from the $1/\cos(\theta)$ behavior by a factor $f\neq 1$ in Eq. (2) is a purely empirical approach [2] which so far has proven to fit data fairly well for $0°<\theta<80°$ (see, e.g., Ref. [16]). For angles close to 90°, obviously data must (and do) deviate even from this behavior [16]. In general, deviations from the $1/\cos(\theta)$ law can be expected for increasing angles if the mean value $(dE/dx)_e$ changes as increasingly long segments of the track come close enough to the surface for electrons to escape. $(dE/dx)_e$ may be changing significantly either by the gradual charge equilibration mentioned above or as a consequence of energy loss of the ion.

Other possible reasons [2] for deviations from the $\cos^{-1}(\theta)$ dependence have to do with the fact that the ion trajectories will deviate from straight lines due to multiple scattering. At grazing angles some fraction of the ions will scatter from the target, but this effect is more significant at lower ion energies. There is also the possibility that, in the cascade leading to the observed electrons, memory may not be totally lost of the initial angular correlations of scattered electrons with respect to the direction of the incoming ion.

For the present experiments ions were selected with charge states close to their equilibrium value for solid strippers. The interpretation of the data should thus be somewhat simplified by avoiding those of the above-mentioned complications which are related to rapidly changing charge states. The ions utilized were protons and fully stripped oxygen at 28 and 126 MeV, respectively (which, at the Brookhaven Tandem, are close to the maximum achievable energies for these ions), and 182 MeV gold with 31 electrons removed. This 182-MeV gold beam has the same energy and charge state as the one utilized to inject the AGS Booster for the Brookhaven relativistic heavy ion program and for the Relativistic Heavy Ion Collider [17].

The aim of the present work was to perform accurate electron yield and angular dependence measurements starting at normal incidence and approaching grazing incidence as closely as possible, and to determine to what extent the use of serrated surfaces could suppress the large yields characteristic of grazing collisions.

We describe the experimental arrangement in Sec. II and present the data and the result of least-square fits in Sec. III. Discussion of the flat-plate data and comparisons with other results are presented in Sec. IV, the serrated-plate results and prospects for higher energies are analyzed in Sec. V, and some conclusions are reached in Sec. VI.

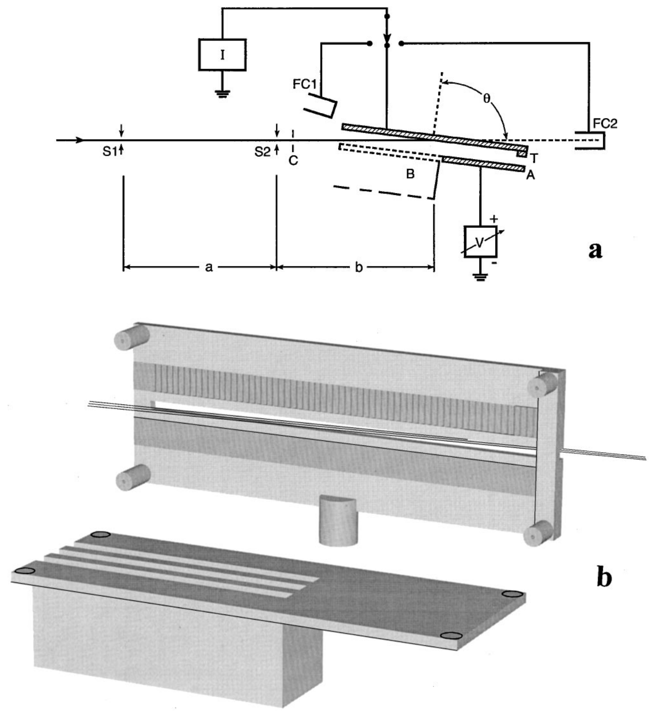

FIG. 1. (a) Schematic diagram of the experimental arrangement. The horizontal scale is distorted. The distance a between the slits $S1$ and $S2$ is 2031 mm, the distance b between $S2$ and the center of plate T is 622 mm, and the length of the plates is 305 mm. See text and Table I for details. (b) Perspective representation of the plate assembly. Plate T is schematically shown as mounted on a large cylindrical insulator, the axis of which is the axis of rotation. In reality this plate was mounted on a stage with insulating adjustment screws for the purpose of alignment. Plate A, shown at the bottom removed from the assembly, was supported by the four small insulating posts shown protruding from plate T.

II. EXPERIMENTAL ARRANGEMENT

Figure 1(a) is a schematic (not to scale) top view of the experimental arrangement. The ion beam comes in from the left through two sets of collimating slits $S1$ and $S2$ and a fixed cleanup aperture C. It either hits the 305-mm-long target plate T, or it continues through a 6.35-mm-high center slot [see Fig. 1(b)] to be measured in the Faraday cup FC2. An anode plate A parallel to T is mounted at 25.4 mm from T on insulating posts. This anode plate has three 9.5-mm-high slots to allow the beam to either go through the slot in T or to hit the surface of T above or below this slot depending on the vertical position of the plate assembly. The anode A is also provided with a box B designed to capture most electrons that may escape through the slots in A, while still allowing the ion beam to get in for all angles $\theta > 55°$ through slots in the front of the box, and for angles around 50°, 40°, 20°, and 0° through the apertures in the side of the box as schematically indicated in Fig. 1(a). These apertures, which are normally provided with covers, are selectively uncovered to obtain data at the desired angles.

The plate assembly is mounted on the center post of a vacuum chamber by means of insulating adjustable alignment screws (not shown). The vertical position of this post can be remotely controlled as well as the angle θ which is measured by means of a digital rotary angle encoder. The position of the target plate T is accurately adjusted so that the axis of rotation is in the plane of the target and the top of the plate is level.

The target plate shown in Fig. 1(b) has two inserts, one of which is flat and the other serrated. The idea was to compare the yields from both types of surfaces in a single measurement. This was done, but the flat-plate data presented in the next section was obtained with a similar but entirely flat plate without inserts. The reason for this is that the alignment and flatness of the inserts were not good enough to allow accurate measurements for angles $\theta > 89.5°$. Thus, for the final data, the plate with the inserts was only used to obtain yields from the serrated surface, for which the last few tenths of a degree are of less interest.

A Faraday cup FC1 can be introduced between the cleanup aperture and the plate assembly. For most measurements the anode plate was positively biased (200 V), and the electron current superimposed with the beam current was measured with an electrometer which was also used to measure currents in the two Faraday cups. Only for the proton beams at angles $\theta < 70°$ was it necessary instead to bias the target T negatively (-200 V), and measure the electron current on the anode A. For those points the electron yield becomes much smaller than 1, and can no longer be accurately measured when added to the much larger beam current.

The pressure in the chamber varied between about 1×10^{-6} and 5×10^{-6} Torr during the measurements. Consistent results were obtained in spite of these variations indicating that for clean stainless steel surfaces and for a clean, cryo-pump-maintained vacuum the secondary electron yields are not pressure sensitive in this range.

The physical dimensions most relevant for the flat-plate measurements are defined and listed in Table I.

TABLE I. Physical dimensions for the flat-plate measurements.

Distance a between slits $S1$ and $S2$	2031 mm
Distance b between $S2$ and the center of rotation	622 mm
Total horizontal opening h_{S1} of slit $S1$	1.0 mm
Total horizontal opening h_{S2} of slit $S2$	0.88 mm
Total length L of the plate T	305 mm
Length L' of the open slot in plate T	279 mm
Height of the slot in plate T	6.35 mm
Flatness tolerance for plate T	± 0.025 mm
Full horizontal beam size at center of plates	1.46 mm
Horizontal angular beam spread	$\pm 0.027°$ ($\pm 1.6'$)

The last two quantities in Table I were computed using the above given slit openings h_{s1} and h_{s2} and the distances a and b [see Fig. 1(a)]. The slits are adjustable and wider openings were used for a number of preliminary measurements. The values shown here correspond to the data presented in the next section for the flat plate. For the less critical serrated plate measurements, slit settings were utilized which were about twice as large as indicated in Table I. The corresponding full horizontal beam size and the horizontal angular beam spread for the serrated plate data are, respectively, 2.8 mm and $\pm 0.05°$.

One problem encountered when attempting precise electron yield measurements closer and closer to grazing incidence angles is that, in spite of tight collimation and long plates, beyond a certain angle the beam spot size on the target will exceed the target length. For the present case the angle for which the beam spreads out over the entire length of the plate is $\theta = 89.73°$ as is easy to compute from the values given in Table I. Unavoidable misalignments may actually cause some of the beam to start missing the target surface at slightly smaller angles. Thus, to get closer to 90° one must devise a system that compensates for such losses or that allows appropriate corrections to be made.

When the beam goes through the slot in the target plate T [see Fig. 1(a)] there should normally be no current measured from this plate until, approaching angles close 90°, some of the beam will no longer go through. Portions of the beam are then intercepted by both the 12.7-mm-wide tab connecting the upper and lower portions of the plate at the left, and by the 12.7-mm-wide vertical bar mounted in contact with the plate surface and covering the end of the slot at the right. The Faraday cup FC2 current is recorded as well as the plate signal. The plate signal is then subtracted from the signal obtained for the same angle when the plate assembly is moved to the up or down positions where the target plate intercepts the full beam. This difference is then a measure of the signal one would obtain solely from the fraction of the beam hitting a length of plate equal to the open length of the slot. The Faraday cup FC2 current previously recorded corresponds precisely to that fraction of the beam, and therefore the yield can be determined. Under these circumstances the useful part of the beam results from further collimation and therefore the effective angular beam spread will in general be even smaller than indicated in Table I.

The above-mentioned subtraction of plate signals is in fact carried out for all angles even though the subtracted signal becomes negligible for angles $\theta < 89.5°$. Small spurious signals, such as those due to residual gas ionization or to electrons originating from the slits, would thus be cancelled.

For the configuration shown in Fig. 1(a) i.e. positive bias applied to the anode A and current measured from the target T, the measured yield at a given angle θ is calculated as follows:

$$\gamma_B(\theta)=q\left(\frac{I_t-I_{t0}}{I_2}-1\right), \tag{3}$$

where q is the charge state, I_t is the target current measured in the up or down position, and I_{t0} the target current measured in the center position with a beam going through the slot, this beam being measured as I_2 in the Faraday cup FC2.

When the yield is much smaller than 1, the signal from the electron current is swamped by the beam current and the accuracy of the measurement then requires the target to be biased negatively and the anode currents to be measured instead of the target currents. Calling the anode currents I_a and I_{a0} for the up or down and for the center positions, respectively, the yield for this configuration is then simply:

$$\gamma_B(\theta)=q\,\frac{I_a-I_{a0}}{I_2}. \tag{4}$$

This configuration was only to be used with angles $\theta<70°$ for the proton data presented in the next section. A careful comparison of earlier data obtained for all angles (also for oxygen and gold) showed a small but consistent difference of about 6% between results obtained with the two configurations consistent with 6% of the electrons from the target being lost and not collected by the anode. Thus a 6% correction was applied to the five proton data points that had to be measured with the second configuration. The only other correction was an ~8% upward adjustment of the three 0° yields required by unavoidable electron losses through the apertures through which the beam enters for this angle (see Fig. 1.). This electron loss was measured at 20° for each case by comparing results obtained by covering and uncovering the 0° apertures. These losses for 0° and for 20° are expected to be identical for all practical purposes.

For each configuration, signal as a function of bias was measured and in both cases saturation was observed beyond 50 or 60 V. The data shown in the next section were obtained with bias voltages of 200 V to ensure as nearly perfect collection as possible.

An optical telescope was used to align the slits and the plate assembly. This telescope was also used to zero the angle encoder with a precision of about 0.1°. To obtain a more accurate adjustment the ratios of beam currents in FC2 and FC1 were plotted, and the zero intercept of a straight line drawn through these data determines the 90° angle with a precision of about ±0.02°. An example of such a plot is shown in Fig. 2.

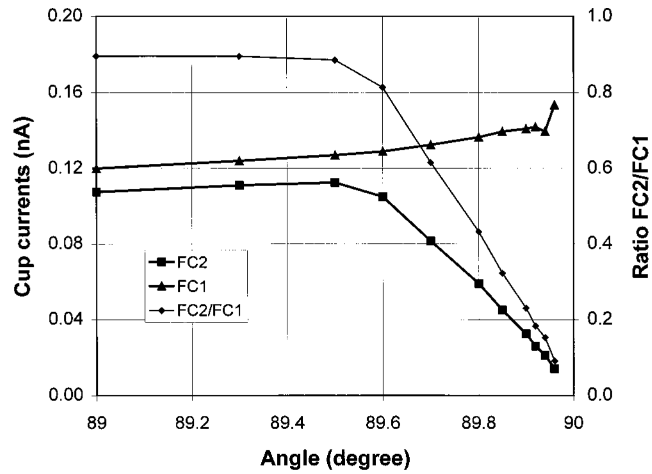

FIG. 2. Example of the plots of Faraday cup currents and their ratio as a function of angles close to 90° utilized to determine the zero for the angle encoder.

III. EXPERIMENTAL RESULTS

The target material studied with these measurements was 304 stainless steel. The density is 8.02 g/cm^3 [18]. The composition of this material can vary slightly around typical values [18]. The values adopted for the interpretation of the data are listed in Table II. For Cr the specified concentration is 18–20%, and 19% was adopted. For Ni, 10% was adopted since the specified concentration is 8–12%. For Mn and Si we adopted half the maximum values of 2% and 1%, respectively. C, P, and S all have concentrations of less than 0.1%, and they were neglected. These small uncertainties in the composition will have negligible impact on the interpretation of the data.

The ion beams used for these experiments are listed in Table III together with some of the quantities characteristic of their slowing down and their angular scattering in stainless steel.

The stainless-steel electron yields as a function of incidence angle obtained in these experiments for the three ion beams listed above are tabulated in Table IV. The data were obtained as described in Sec. II except that, for the flat plate, average yield values from the ''up'' and ''down'' positions are used. These yields should in principle be identical. The use of these averages reduces random errors due, e.g., to beam fluctuations and, to first order, eliminates a possible systematic error due to small plate rotations coupled to the vertical displacements.

Least-square fits were performed for the flat-plate data between 0° and 89° to obtain estimates of the parameters in Eq. (2) in Sec. I. Figure 3 shows double logarithmic plots of the yields as functions of the cosine of the angles. Deviations from the behavior described by Eq. (2) are seen as departures from straight lines. The fits are quite good for most of the angular range, and the deviations are discussed in the next

TABLE II. Composition of 304 stainless steel [18].

Element	Composition of #304 SS (% in weight)
Fe	69.5 ± 4.5
Cr	19.0 ± 1.0
Ni	10.0 ± 2.0
Mn	1.0 ± 1.0
Si	0.5 ± 0.5

TABLE III. Ion beams used and their interaction with stainless steel.

Ion	Proton (^{1}H)	Oxygen (^{16}O)	Gold (^{197}Au)
Energy (MeV)	28	126	182
Energy (MeV/amu)	28	7.9	0.92
Charge state	1+	8+	31+
Electronic stopping power, S_E (MeV cm^2/mg)	0.01342	2.093	53.81
Elastic stopping power, S_N (MeV cm^2/mg)	5.8×10^{-6}	0.001 17	0.57
Linear energy transfer, (LET) (MeV cm^2/mg)	0.01342	2.094	54.38
S_N/LET (%)	0.043	0.056	1.05
Range (μm)	1490	51.5	7.73
Mean-square scattering angle[a] for 1 μm (°/μm)	0.22	0.54	0.98

[a]This is the calculated mean-square scattering angle [19] after 1 μm of material for the trajectory projected onto a plane containing the incoming trajectory. For small scattering angles their mean-square values will scale approximately as the square root of the thickness.

section. The parameters resulting from this fitting procedure are listed in Table V. The tabulated uncertainties are the purely statistical standard deviations resulting from the least-square fitting procedure.

Here the parameters Λ_B, as defined before, are the ratios $\gamma_B(0°)/S_E$ where S_E are the electronic stopping powers listed in Table III. The coefficients C_B are the parameters Λ_B normalized to 1.0 for protons. They are thus a measure of the

TABLE IV. Secondary electron yields (electrons per ion) measured for proton, oxygen, and gold beams incident on flat and serrated stainless-steel plates for different angles of incidence θ. Normal incidence corresponds to $\theta=0°$.

θ (degree)	28-MeV protons Flat	28-MeV protons Serrated	126-MeV oxygen Flat	126-MeV oxygen Serrated	182-MeV gold Flat	182-MeV gold Serrated
0.00	0.14	0.21	17	24	209	351
20.00	0.14	0.37	18	36	223	578
40.00	0.18	0.66	22	46	275	537
50.00	0.23	0.40	27	18	325	251
60.00	0.32	0.40	33	17	410	255
70.00	0.47	0.43	49	19	598	265
75.00	0.65	0.53	62	20	751	270
80.00	0.96	0.92	93	21	1110	283
82.00	1.23	1.02	117	23	1339	279
84.00	1.73	1.20	150	25	1758	274
85.00	2.18	1.23	174	25	2118	303
86.00	2.92	1.36	218	25	2645	306
86.50	3.52	1.40	247	27	2965	309
87.00	4.18	1.59	282	27	3497	297
87.50	5.24	1.68	341	30	4282	363
88.00	6.86	1.84	422	30	5386	330
88.50	8.93	1.91	591	32	7269	337
89.00	13.68	1.96	967	36	10638	356
89.30	19.54	2.02	1460	42	13457	396
89.50	26.34	2.10	2210	47	16862	393
89.60	32.41	2.17	2696	51	19114	392
89.70	42.16		3387		23130	
89.80	62.12		4479		26558	
89.85	79.71		5537		30755	
89.90	99.59		6112		32414	
89.92	102.43		6461		32757	
89.94	113.13				30539	
89.96	147.81				28046	

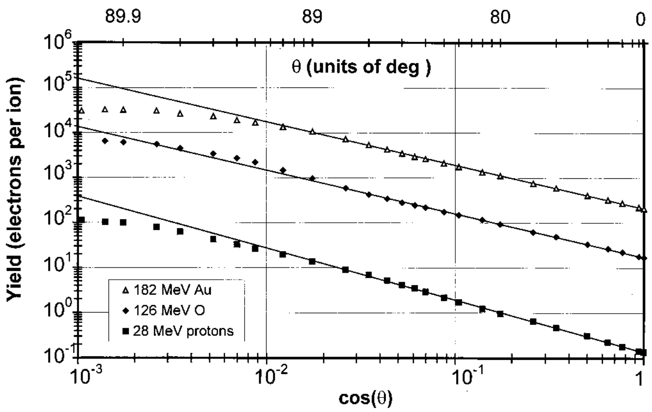

FIG. 3. Doubly logarithmic plot of the flat plate yields listed in Table IV, vs cos(θ). The straight lines are results of least-square fits of the data between 0° and 89° to the functional form given in Eq. (2) with the resulting parameters listed in Table V.

so-called electron yield ''deficit'' with respect to the simplest predictions based on the proton results (see Sec. I).

Figures 4, 5, and 6 show the data for the individual ion species. In each case the flat-plate results are compared with the serrated-plate results. These plots are linear in the angle of incidence. The lines joining the points for the serrated-plate data are for guiding the eye, and the lines for the flat plate are calculated with Eq. (2) using the parameters listed in Table V.

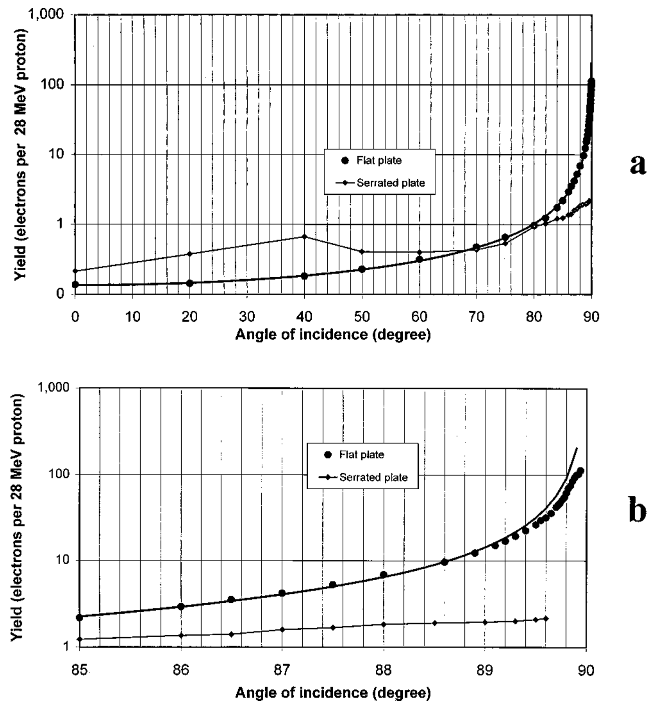

FIG. 4. Secondary-electron yields vs angle of incidence for 28-MeV protons striking a flat and a serrated stainless-steel surface. (b) An expanded view of the last 5°.

IV. DISCUSSION OF THE FLAT-PLATE DATA AND COMPARISON WITH OTHER RESULTS

First we shall compare our proton results with the normal incidence yields obtained by others for various materials. Table VI lists Λ_B values together with the corresponding beam energies or energy ranges. Far from a comprehensive review this is only a comparison of some of the more relevant data.

One sees, as mentioned before, that the values of Λ_B have proven to be fairly constant for each material in experiments covering wide energy ranges. There apparently are no proton data beyond 67 MeV. However, if one assumes that Λ_B will remain approximately constant up to 1 GeV then, using our results, one can estimate the electron yield for SS at that energy. The value of the electronic stopping power $(dE/dx)_e$ is calculated [19] to be 1.61×10^{-3} MeV cm^2/mg. Then assuming that the value of Λ_B remains constant at 10.1 mg/(MeV cm^2), we get an estimate of 0.016 electrons per 1-GeV proton for the yield at normal incidence on a 304 stainless-steel surface.

Our oxygen and gold beam results are in line with the well-known fact [2] that for heavier and heavier ions secondary-electron yields per unit linear energy transfer (LET) deviate increasingly from the proton values. In other words, as can be seen from Table V, $1>C_B(O)>C_B(\mathrm{Au})$ which means that the heavier ions are less efficient in converting into secondary electrons some of the energy deposited in the surface layer. More detailed comparisons with other results are difficult since data are still rather sparse, in particular for the higher beam energies, and the parameter space is very large considering the possible combinations of ion species, beam energies, and target materials.

Of the several possible explanations for the electron ''deficit'' for heavier ions, one of the most frequently mentioned is based on the very thin escape zone and on the fact that charge state equilibrium cannot be reached within that layer. This preequilibrium near-surface stopping power concept [9] cannot explain our heavy ion results, in particular not the ones for gold. In this case the incoming charge state of 31+ is much higher than the ''effective'' charge state ~19+ deduced from the bulk stopping power data. So, if stopping power and consequently electron emission scale as the square of the charge, one should naively expect an en-

TABLE V. parameters resulting from least-square fitting of the data (see text).

Ion beam	$\gamma_B(0°)$	f	Λ_B (mg/MeV cm^2)	C_B
28-MeV protons	0.135 ± 0.003	1.152 ± 0.008	10.06	1.0
126-MeV oxygen	16.96 ± 0.30	0.969 ± 0.008	8.10	0.805
182-MeV gold	208.1 ± 2.5	0.962 ± 0.005	3.87	0.385

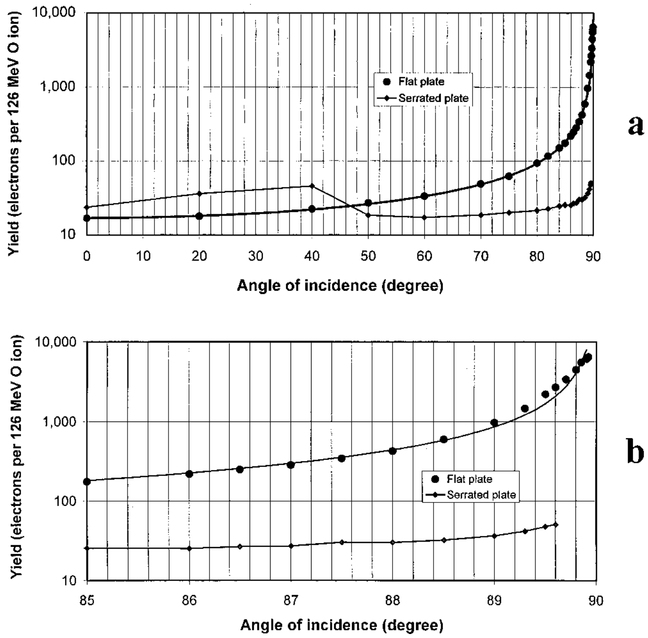

FIG. 5. Secondary-electron yields vs angle of incidence for 126-MeV 8+ oxygen ions striking a flat and a serrated stainless-steel surface. (b) An expanded view of the last 5°.

hancement of ~2.7 rather than the observed deficit (C_B $=0.38$, Table V). Clearly, at least for this ion-target combination, other factors must be responsible for the deficit.

We finally turn to the results for the incidence angle dependence of the yield, the study of which was the main thrust of the present work. Very few relevant references were found and the one covering the widest angular range [16] shows results ranging from 0° to only 85° obtained with various 40-keV ions on a copper target. Another experiment [23], using 100-MeV Si ions on various metallic targets and on silicon, was limited to an angular range from 10° to 70°.

As seen most clearly from fig. 3, we find excellent agreement with the angular dependence described by Eq. (2) over an angular range $89° > \theta > 0°$ which, compared to previous experiments [16,23], extends to angles much closer to 90°. To see if the deviations observed for angles starting at ~89° could be due to the multiple scattering or energy loss mechanisms mentioned in Sec. I, we will first try to estimate these effects at $\theta = 89°$:

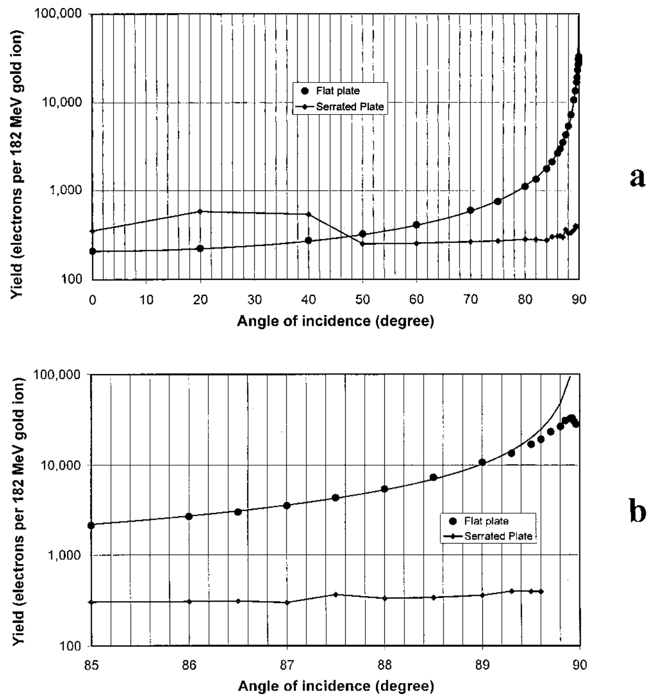

FIG. 6. Secondary-electron yields vs angle of incidence for 182-MeV 31+ gold ions striking a flat and a serrated stainless-steel surface. (b) An expanded view of the last 5°.

We must first calculate the length of that part of the trajectory which is within the surface layer from which electrons may escape. The thickness of this layer was estimated to be roughly 30 Å for a carbon target [8]. Since it is the electrons in the material that are responsible for stopping the escaping electrons, it is reasonable to reduce this escape depth from carbon to SS by the ratio of their electron densities. This ratio is roughly equal to 0.3, which leads to an escape depth for SS of about 9 Å. The corresponding path length within the escape zone is thus 9 Å/cos(89°) = 516 Å $\approx 0.05\ \mu$m. This path length is so small compared to even the smallest ion range (7.7 μm for the gold beam, see Table III) that changes in LET during ion penetration cannot account for the observed effect. The calculated multiple scattering angles for 1 μm (see Table III) are also so small that angular changes of individual trajectories are unlikely to ac-

TABLE VI. Comparison of some of the electron yield data for normal incidence of energetic protons on various materials.

Target material	Energy (MeV)	$\Lambda_B = \gamma_B/(dE/dx)_e$ mg/(MeV cm^2)	References
C	0.02–7.5	5.0	Ref. [13]
Al_2O_3	15–67	9.4 ± 0.6	Calculated from data in Ref. [14]
Au	5–18	22 ± 3	Calculated from data in Ref. [20]
Al	4–12	3.6	Calculated from data in Refs. [21]
Cu		7.3	and [22]
Ag		13.1	
Au		18.9	
304 stainless steel	28	10.1 ± 0.3	Present work

TABLE VII. Calculated mean-square projected scattering angles [19] of the three ions used in the experiment after penetrating half of the electron escape depth at 89.9° incidence.

Ion beam	Scattering angle
28-MeV protons	0.047°
126-MeV oxygen	0.086°
182-MeV gold	0.556°

count for an appreciable part of this effect in the vicinity of 89°.

We turn now to the maximum in the yield curve which we observed for the gold data around 89.9° [see Fig. 6(b)]. Svensson, Holmén, and Burén [16] using 40-keV protons, had observed maxima in their yield vs angle curves at angles between 78° and 82° for the various target materials. They suggest that these maxima could be correlated with the angles at which sputter yield maxima occur. Repeating the calculation of these maximum sputter yield angles for the ions used in the present experiments we should expect maximum secondary-electron yields at 88.5° for the gold beam, at 88.9° for the oxygen beam, and at 89.0° for the protons. It is clear from Table IV and Figs. 4–6 that in our data the only maximum observed is at ~89.9 for the gold beam, and that there are no maxima at least up to 89.92° for oxygen and 89.96° for protons. Either the suggested correlation, for some reason, stops working at the higher energies, or the effect observed by Svensson, Holmén, and Burén was due to other physical or instrumental effects.

We will now see if the maximum we observed at 89.9° for the gold beam could be due to multiple scattering. For a particle incident at 89.9° the path length within the ~9-Å-deep surface layer which corresponds to the electron escape zone is 9 Å/cos(89.9°) = 0.52 μm if multiple scattering can be neglected. If multiple scattering is not negligible, then some of the ions will be driven faster into the bulk of the material, some will be driven out and ''reflected,'' and a very small number may stay longer within the escape zone. The overall effect will be a reduction of the electron yield. To evaluate the possible effects of multiple scattering on the electron yields around 89.9° we calculate for each of the ion beams the mean-square scattering angle after the first half of the escape zone is penetrated, i.e., after 0.26 μm (see Table VII).

Without attempting a detailed quantitative argument we see that only for the gold beam is the multiple scattering very significant at this angle. For oxygen the ions must travel through half the escape zone before the mean-square angle becomes comparable to $90° - \theta$ and therefore the effect will be small, and it will be even smaller for protons. We therefore conclude that multiple scattering may be a plausible explanation for having observed a maximum only for the gold beam, even though we, of course, realize that these arguments get more complicated if surface topography is considered.

It should finally be mentioned that a number of recent publications (see, e.g., Refs. [24], [25]) present predictions and results for grazing collisions but only low-energy (<1 MeV) experimental data were available and total electron yields are not always addressed. Hopefully our results will stimulate calculations for higher energies, which may then serve to obtain better extrapolations to, e.g., 1 GeV protons.

TABLE VIII. Comparison of near grazing incidence secondary-electron yields for the flat and serrated plates with 45° incidence yields on the flat plate.

Ion beam	Flat-plate yield at 89.6°	Serrated-plate yield at 89.6°	Flat-plate yield at 45°
28-MeV protons	32.4	2.17	0.21
126-MeV oxygen	2696	50.6	24.7
182-MeV gold	19114	392	300

V. DISCUSSION OF THE SERRATED-PLATE DATA AND PROSPECTS FOR HIGHER ENERGIES

The idea of reducing grazing incidence secondary electron yields by replacing flat electrodes by serrated surfaces is based on the following facts.

(a) For the accelerator applications of interest, most of the ions causing the secondary electrons (e.g., halo particles), far from being istropically distributed in space, are instead highly collimated within a small solid angle centered on the main beam direction.

(b) Most of the surface area defining the individual teeth of such a serrated plate is inclined with respect to the incoming ion trajectories by large angles (±45° for our experiment).

(c) The backward secondary electron yield at the impact point with such an inclined surface is much smaller than at grazing incidence with a flat plate. But of course electrons will also be generated at the exit points for ions penetrating the teeth and at subsequent impact points, etc.

To see to what extent our data confirm such yield reductions we compare in Table VIII grazing incidence on both types of surfaces with 45° flat-plate results. For grazing incidence we selected 89.6° from Table IV, which is the largest angle for which we have useful serrated-plate data. The 45° yields shown in Table VIII were obtained by linear interpolation between the 40° and 50° values in Table IV.

We see that, at 89.6°, the serrated-plate yields are indeed much smaller than the flat-plate yields, but not as small (especially for protons) than the flat-plate yields at 45°. It is easy (neglecting multiple scattering) to calculate from the ranges listed in Table III, and from the geometry indicated in Fig. 7(a) with $s = 2\,h = 12.7$ mm, that 28-MeV protons incident at an angle $\theta = 89.6°$ will traverse three or four teeth before stopping. This would correspond to seven or nine traversals of solid-vacuum boundaries. Considering that exit yields are generally somewhat larger than entrance yields (Meckbach factors of ~1.3 are common), and the fact that LET values increase as the protons slow down, it is not surprising to find the serrated-plate yield ~10 times larger than the flat-plate yield at 45°. In fact, an even larger yield would be expected if it were not for multiple scattering causing

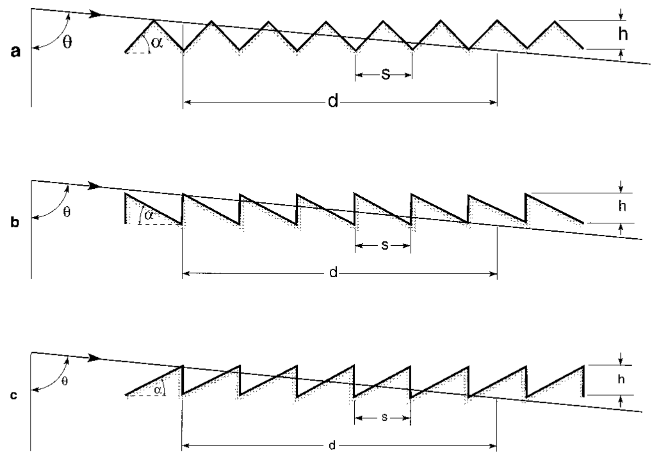

FIG. 7. Schematic cross sections of serrated-plate surfaces used as examples for yield estimates (see text). (a) $s=2h=12.7$ mm corresponds to the serrated plate used in the present experiments.

considerable deflection after a few 100 μm of penetration (see Table III). No attempt was made at performing a Monte Carlo-type calculation to take this effect into account. Finally, it should be mentioned that the surface polish of the serrations is not quite as good as for the flat plate, and this fact will also affect the comparison.

Similar considerations applied to the oxygen and gold beams show that at 89.6° only a fraction of these ions ($\sim$29% for oxygen and $\sim$5% for gold) will manage to traverse a single tooth (three interface traversals) while the rest are stopped after penetrating the first surface. Also, the geometry that would need to be considered is no longer as simple as indicated in Fig. 7(a) because now the ranges are comparable to the radius of curvature characteristic of the upper edges of the serration teeth. Thus, grazing (high yield) collisions close to these edges become more significant. In view of these considerations, and without attempting detailed estimates, it seems that the values shown in Table VIII are also very reasonable for the oxygen and gold beams.

Finally we will attempt to provide estimates of serrated surface electron yields for the case of 1-GeV protons, to see if this is a promising approach for the SNS collimator design [26]. From what we have learned, it should indeed be easier to perform valid calculations at this energy since multiple scattering and energy loss will be less important, and can at first be neglected. For simplicity we will also assume a $1/\cos(\theta)$ angular yield dependence, which for the present purpose is close enough to behavior observed at lower energies (see Table V).

We performed calculations for the three serration-teeth geometries illustrated in Figs. 7(a), 7(b), and 7(c) to evaluate possible effects of different shapes on secondary emission performance. Considering first the case illustrated in Fig. 7(a), and calling $\pm\alpha$ the inclination of the serration surfaces, s the distance between teeth, h the depth of the teeth, and d the longitudinal distance for a particle coming in at an incident angle θ to penetrate through a depth h, we can write

$$d=h\tan(\theta), \tag{5}$$

$$s=\frac{2h}{\tan(\alpha)}. \tag{6}$$

Calling N the number of teeth traversed, we get

$$N=\frac{d}{s}=\frac{\tan(\alpha)\tan(\theta)}{2}, \tag{7}$$

which for large N is also approximately equal to the number of incoming and the number of outgoing surface traversals of the particle before it gets buried in the bulk of the electrode. Calling γ_{TB} and γ_{TF} the total backward and forward (incoming and outgoing) electron yields for the N transitions, we get with the above-mentioned assumptions:

$$\gamma_{\mathrm{TB}}=N\frac{\gamma_0}{\cos(\theta-\alpha)}, \tag{8}$$

$$\gamma_{\mathrm{TF}}=-N\frac{M\gamma_0}{\cos(\theta+\alpha)}, \tag{9}$$

where γ_0 is the normal incidence backward yield, and M is the Meckbach factor, i.e., the enhancement of forward vs backward yield.

From Eqs. (7), (8) and (9) we get the total $\gamma_T=\gamma_{\mathrm{TB}}+\gamma_{\mathrm{TF}}$:

$$\gamma_T=\gamma_0\frac{\tan(\alpha)\tan(\theta)}{2}\left(\frac{1}{\cos(\theta-\alpha)}-\frac{M}{\cos(\theta+\alpha)}\right). \tag{10}$$

For angles close to grazing incidence, i.e., $\theta\to 90°$ we get

$$\gamma_T\to\gamma_0\frac{\tan(\alpha)}{2\cos(\theta)}\,\frac{1+M}{\sin(\alpha)},$$

$$\gamma_T\approx\gamma_0\frac{1+M}{2\cos(\alpha)\cos(\theta)}. \tag{11}$$

Comparing to the yield γ_{flat} from a flat plate at the same incident angle we get

$$\frac{\gamma_T}{\gamma_{\mathrm{flat}}}=\frac{1+M}{2\cos(\alpha)}. \tag{12}$$

Since $M>1$ (typically 1.3 or 1.5) and $\cos(\alpha)<1$ we see that this ratio is always larger than 1 and therefore we would get more secondary electrons from the serrated plate. Note that this result is independent of the absolute yield for normal incidence and depends only on the $1/\cos(\theta)$ assumption for the angular dependence and on the approximations of negligible change in $(dE/dx)_e$ and negligible scattering while penetrating the serration depth.

The same approach was followed for the geometry shown in Fig. 7(b) where the entrance face of the serration teeth is perpendicular to the overall electrode surface. In this case we get

$$\frac{\gamma_T}{\gamma_{\text{flat}}}=\tan(\alpha)+\frac{M}{\cos(\alpha)}. \tag{13}$$

We see that for small values of α the limit of this expression is M, which is larger than 1. Again, there is no advantage in using a serrated plate. By inverting the teeth [see Fig. 7(c)] we get

$$\frac{\gamma_T}{\gamma_{\text{flat}}}=M\tan(\alpha)+\frac{1}{\cos(\alpha)}. \tag{14}$$

This is better, since now the same yield as obtained from a flat plate can be approached for small angles α. In a practical application the smallest allowable α is determined by the angular distribution of the incident particles since an abundance of grazing collision on the inclined teeth surfaces would defeat the purpose of a serrated surface. For, e.g., $\alpha=10°$ and $M=1.5$ we get $\gamma_T/\gamma_{\text{flat}}=1.28$. The serrated-plate performance is still slightly worse when compared to the flat plate as also indicated by the dotted lines in Fig. 8.

What will change this situation is multiple scattering. The increasing amount of serrated-plate teeth material traversed as 90° incidence angles are approached is orders of magnitude larger than the thin escape zone material traversed in the flat plate for the same angles. So multiple scattering will interrupt the yield increase for the serrated plate much sooner than for the flat plate. To estimate at what incidence angle this will happen we select as example serrations such as the ones depicted in Fig. 7(c) with $h=5$ mm and $\alpha=10°$, and we calculate the mean-square scattering angle after a distance $d/2$, when half the teeth have been penetrated. For this example TRIM calculations [19] for 1-GeV protons in 304 SS indicate that this scattering angle becomes equal to the angle $90°-\theta$ between the surface and the incoming trajectory when $\theta=89.3°$. Thus, beyond ~89.3° we can expect that the straight line increase indicated by the dotted lines in Fig. 8 will not continue. For this angle, $d/2\approx 20$ cm and the equivalent thickness of SS traversed at the $d/2$ point is ~5 cm with an energy loss of 65 MeV. The range of 1-GeV protons in stainless steel is ~57 cm. Preliminary results from Monte Carlo-type calculations [27] tend to confirm these estimates.

We conclude that replacing smooth by serrated electrodes can be effective in reducing the secondary-electron emission. In the case of our application of collimators for 1-GeV protons, the tradeoff will be a slight increase in the penumbra of partially degraded protons. The design of the surface and the degree of the achievable electron reduction will depend on the angular distribution of the incident protons. For example, if the protons are restricted to an ~1° angular range between 89° and 90° then the 5-mm serrations described above should be quite effective. For wider incident distributions or for even better electron suppression deeper serrations may be required. Compared to similar electron reduction schemes [28], where the multiple scattering and collimating functions are separated, the present solution is probably more effective and it does encroach less on the useful collimator aperture.

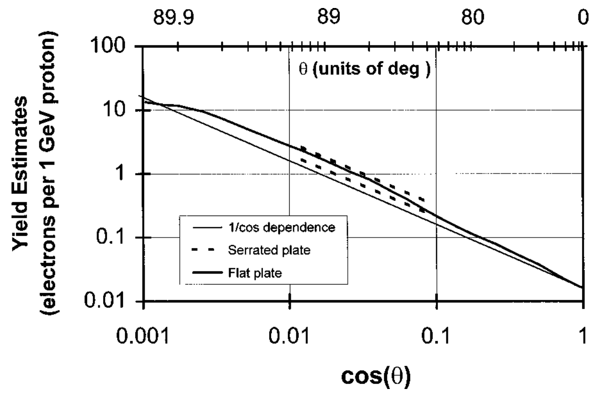

FIG. 8. Estimated electron yields for 1-GeV protons incident on smooth (solid lines) and serrated (dotted lines) SS surfaces. The curved line represents the present data scaled from 28 MeV to 1 GeV by the ratio of the respective stopping powers. The straight solid line shows a $\cos^{-1}(\theta)$ angular dependence. The dotted lines correspond to a serrated plate such as depicted in Fig. 7(c) with a tooth height $h=5$ mm and $\alpha=10°$ (see text). The upper and lower dotted lines were obtained assuming $\cos^{-1.152}(\theta)$ and $\cos^{-1}(\theta)$ angular dependencies, respectively. The left termination of these dotted lines indicates the incidence angle at which the calculated [19] mean-square multiple scattering angle will be equal to $90°-\theta$ after only half the involved teeth have been penetrated. The actual yield at this angle will already be reduced compared to what is shown, and beyond this angle strong multiple scattering effects will limit any further yield increase.

VI. CONCLUSIONS

Angular accuracy unprecedented for this type of measurements, as well as a much longer target, and an effective system for compensating for lost beam at grazing angles, allowed electron yield measurements for incidence angles much closer to 90° than hitherto possible. Near $1/\cos(\theta)$ behavior was observed between 0° and 89° and the deviations from this behavior were accurately determined as well as the normal incidence yields. For 28-MeV protons the electron yield is closely approximated by $0.135/\cos(\theta)^{1.152}$ for $0°<\theta<89.5°$.

Rather large grazing incidence yields of up to ~33 000 electrons per ion were measured for the 1-MeV/amu gold beam, as expected from previous observations at accelerator related systems [6]. These data are thus directly relevant for practical applications. Together with the proton and oxygen data they should also be useful in extending and verifying existing or new theoretical descriptions, thus enhancing the understanding of the underlying phenomena and allowing more reliable predictions and extrapolations which are important for future accelerator applications.

Based on the present proton data, a preliminary estimate was obtained of 0.016 electrons per 1-GeV proton for the yield at normal incidence on stainless steel. This result is of interest for the collimators being designed for the SNS facility. Using appropriately designed serrated surfaces in these collimators may solve the problem if the ~$1/\cos(\theta)$ angular dependence leads to excessive electron production for grazing collisions of halo particles.

The present experiments can of course be extended to other materials, and coatings that have been suggested [29,30] for the reduction of electron produced secondary electrons will be investigated. Also further improvements are possible in angular accuracy and in the small angle limit for these measurements. It would be of particular interest to find maxima for the oxygen and proton data and to compare their positions with the maximum found here for the gold beam at ~89.9°. A more precise goniometer would be required to move the plate assembly, and the surface of the target would need to be machined or ground and polished to even higher accuracy.

ACKNOWLEDGMENTS

This work was performed under the auspices of the U.S. Department of Energy. We would like to thank W. W. Weng for his encouragement and support, M. Manni for the detailed design and for supervising the fabrication of the hardware, D. A. Graham and H. F. Abendroth for assistance with electronics and computers, C. W. Carlson for his help with the alignment, and the BNL Tandem crew for providing the ions and invaluable support.

[1] J. Devooght, J. C. Dehaes, A. Dubus, M. Cailler, J. P. Ganachaud, M. Rosler, and M. Brauer, in *Particle Induced Electron Emission I*, edited by G. Hohler and E. A. Niekish, Springer Tracts in Modern Physics Vol. 122 (Springer-Verlag, Berlin, 1991).

[2] D. Hasselkamp, H. Rothard, K. O. Groeneveld, J. Kemmler, P. Varga, and H. Winter, in *Particle Induced Electron Emission II*, edited by G. Hohler and E. A. Niekish, Springer Tracts in Modern Physics Vol. 123 (Springer-Verlag, Berlin, 1991)

[3] H. Rothard, Scanning Microsc. **9**, 1 (1995).

[4] *Ionization of Solids by Heavy Particles*, Vol. 306 of *NATO Advanced Study Institute, Series B: Physics*, edited by R. Baragiola (Plenum, New York, 1993).

[5] W. T. Weng *et al.*, in *Proceedings of the Particle Accelerator Conference, Vancouver, 1997*, edited by M. Comyn, M. K. Craddock, M. Reiser, and J. Thomson (IEEE, New York, 1998), pp. 970–972.

[6] S. Y. Zhang, in *Proceedings of the 1999 Particle Accelerator Conference, New York, 1999*, edited by A. Luccio and W. MacKay (IEEE, New York, 1999), pp. 3297–3299.

[7] Y. Chanut, J. Martin, and R. Salin, Surf. Sci. **106**, 563 (1981).

[8] M. Jung, H. Rothard, B. Gervais, and J. P. Grandin, Phys. Rev. A **54**, 4153 (1996).

[9] H. Rothard, J. Schou, and K. O. Groeneveld, Phys. Rev. A **45**, 1701 (1992).

[10] H. Rothard, C. Caraby, A. Cassimi, B. Gervais, J. P. Grandin, P. Jardin, and M. Jung, Phys. Rev. A **51**, 3066 (1995).

[11] E. J. Sternglass, Phys. Rev. **108**, 1 (1957).

[12] W. Meckbach, G. Braunstein, and N. Arista, J. Phys. B **8**, L344 (1975).

[13] H. Rothard, M. Jung, M. Caron, J. P. Grandin, B. Gervais, A. Billebaud, A. Clouvas, and R. Wunsch, Phys. Rev. A **57**, 3660 (1998).

[14] C. M. Castaneda, L. McGarry, C. Cahill, and T. Essert, Nucl. Instrum. Methods Phys. Res. B **129**, 199 (1997).

[15] H. Rothard, K. Kroneberger, A. C. Clouvas, E. Veje, P. Lorenzen, N. Keller, J. Kemmler, W. Meckbach, and K. O. Groeneveld, Phys. Rev. A **41**, 2521 (1990).

[16] B. Svensson, G. Holmén, and A. Burén, Phys. Rev. B **24**, 3749 (1981).

[17] T. Roser, in *Fourth European Particle Accelerator Conference, London, 1994*, edited by V. Suller (Ch. Petit-Jean-Genaz, 1994), pp. 151–155.

[18] *Handbook of Chemistry and Physics*, 71st ed. (CRC, Boca Raton, FL, 1991), pp. 12–122.

[19] Calculated using an updated version of the TRIM program. J. F. Ziegler and J. P. Biersack, *The Stopping Power and Ranges of Ions in Matter* (Pergamon, New York, 1985).

[20] J. E. Borovsky, D. J. McComas, and B. L. Barraclough, Nucl. Instrum. Methods Phys. Res. B **30**, 191 (1988).

[21] D. Hasselkamp, S. Hippler, A. Scharmann, and T. Schmehl, Ann. Phys. (Leipzig) **7**, 555 (1990).

[22] A. Koyama, T. Shikata, and H. Sakairi, Jpn. J. Appl. Phys. **20**, 65 (1981).

[23] R. S. Chauhan, V. K. Mittal, T. K. Nandi, A. Mandal, and D. K. Avasthi, Vacuum **48**, 1031 (1997).

[24] M. L. Martiarena, E. A. Sánchez, O. Grizzi, and V. H. Ponce, Phys. Rev. A **53**, 895 (1996).

[25] M. S. Gravielle, Phys. Rev. A **58**, 4622 (1998).

[26] H. Ludewig, N. Simos, J. Walker, P. Thieberger, A. Aronson, J. Wei, and M. Todosow, in *Proceedings of the 1999 Particle Accelerator Conference* (Ref. [6]), pp. 548–550.

[27] V. Zajic and P. Thieberger (unpublished).

[28] N. N. Catalan Lasheras, F. Ferioli, J. B. Jeanneret, R. Jung, and T. Trenkler, in *Proton Collimation in TeV Colliders*, Proceedings of the Near Beam Physics Symposium, 1997, edited by R. A. Carrigan, Jr. and N. V. Mikhov (Fermilab, Batavia, IL, 1998), pp. 117–126; see also LHC Project Report 156, Geneva, Oct. 1997 (unpublished).

[29] O. Brüning, F. Caspers, I. R. Collins, O. Gröbner, B. Henrist, N. Hilleret, J.-M. Laurent, M. Morvillo, M. Pivi, F. Ruggiero, and X. Zhang, in *Proceedings of the 1999 Particle Accelerator Conference* (Ref. [6]), pp. 2629–2631.

[30] K. Kennedy, H. Harteneck, G. Millos, M. Benapfl, F. King, and R. Kirby, in *Proceedings of the 1997 Particle Accelerator Conference* (Ref. [6]), pp. 3568–3570.